

1       **Investigating the impact of land surface characteristics on monsoon**  
2       **dynamics with idealized model simulations and theories**

3                   Jane E. Smyth\* and Yi Ming<sup>†</sup>

4       *Program in Atmospheric and Oceanic Sciences, Princeton University, Princeton, NJ*

5   \**Corresponding author address:* Jane E. Smyth, Program in Atmospheric and Oceanic Sciences,  
6   300 Forrester Rd., Princeton, NJ 08540.

7   E-mail: jsmyth@princeton.edu

8   <sup>†</sup>Geophysical Fluid Dynamics Laboratory/NOAA, 201 Forrester Road, Princeton, NJ 08540.

## ABSTRACT

9 Monsoons emerge over a range of land surface conditions and exhibit vary-  
10 ing physical characteristics over the seasonal cycle, from onset to withdrawal.  
11 Systematically varying the moisture and albedo parameters over land in an  
12 idealized modeling framework allows one to analyze the physics underlying  
13 the successive stages of monsoon development. To this end we implement  
14 an isolated South American continent with reduced heat capacity but no to-  
15 pography in an idealized moist general circulation model. Irrespective of the  
16 local moisture availability, the seasonal cycles of precipitation and circulation  
17 over the South American monsoon sector are distinctly monsoonal with the  
18 default surface albedo. The dry land case (zero evaporation) is characterized  
19 by a shallow overturning circulation with vigorous lower-tropospheric ascent,  
20 transporting water vapor from the ocean. By contrast, with bucket hydrology  
21 or unlimited land moisture the monsoon features deep moist convection that  
22 penetrates the upper troposphere. A series of land albedo perturbation experi-  
23 ments indicates that the monsoon strengthens with the net column energy flux  
24 and the near-surface moist static energy with all land moisture conditions.  
25 When the land-ocean thermal contrast is strong enough, inertial instability  
26 alone is sufficient for producing a shallow but vigorous circulation and con-  
27 verging a large amount of moisture from the ocean even in the absence of  
28 land moisture. Once the land is sufficiently moist, convective instability takes  
29 hold and the shallow circulation deepens. These results have implications for  
30 monsoon onset and intensification, and may elucidate the seasonal variations  
31 in how surface warming impacts tropical precipitation over land.

## 32 1. Introduction

33 Monsoon circulations play a key role in Earth’s climate, including the atmospheric energy, mois-  
34 ture, and momentum budgets. They are the defining feature of the seasonal cycle over tropical land,  
35 producing rain in local summer and dry conditions in winter. Consequently, monsoon variability  
36 carries great social and economic significance, with agriculture, energy systems, and ecosystem  
37 health all depending on monsoon regularity. Over 70% of the world’s population is directly im-  
38 pacted by monsoon variability, which can cause droughts, floods, food insecurity, worsened wild-  
39 fires, energy shortages, and broad financial impacts (An et al. 2015).

40 The theoretical and societal importance of monsoons has motivated sustained research efforts  
41 to identify the key mechanisms underlying their development and regulation. The traditional con-  
42 ception of monsoons as land-sea breezes has given way to the modern perspective of monsoons  
43 as an integral component of the global atmospheric circulation and climate. Studies applying the  
44 axisymmetric theory for the Hadley cells to idealized monsoons have driven this shift in thinking  
45 (Privé and Plumb 2007a,b; Bordoni and Schneider 2008). Based on theory for angular momentum  
46 conserving circulations, Privé and Plumb (2007a,b) link the meridional extent of the monsoonal  
47 overturning cell to the near-surface maximum of subcloud moist static energy (MSE), and find  
48 that this is a good indicator of the monsoon extent even when zonal symmetry is broken. They  
49 utilize the MITgcm with Newtonian cooling and prescribed SSTs. Bordoni and Schneider (2008)  
50 describe a rapid summertime transition to off-equatorial tropical convergence in an idealized moist  
51 aquaplanet model with a two-stream gray radiation scheme. This indicates that land-sea thermal  
52 contrast is not fundamental to monsoon emergence. They characterize monsoons as a regime tran-  
53 sition of the Hadley circulation: during the monsoon season, the cross-equatorial winter Hadley  
54 cell is in an angular momentum-conserving regime, subject to little influence by extratropical

55 eddies. The alignment of streamlines with angular momentum contours over the Indian mon-  
56 soon sector suggests the potential utility of this theory for off-equatorial monsoons (Bordoni and  
57 Schneider 2008).

58 There are three primary theoretical conceptions of monsoons in the literature: one based on  
59 convective quasi-equilibrium (CQE), another founded on the MSE budget, and one that frames  
60 the monsoon as an extension of the zonal-mean ITCZ (Hill 2019). In the CQE view, the mon-  
61 soonal overturning cell extends to the latitude of highest near-surface MSE, with the maximum  
62 rainfall located just equatorward thereof (e.g. Privé and Plumb 2007a,b; Nie et al. 2010; Hurley  
63 and Boos 2013). CQE posits that convection couples near-surface and upper tropospheric MSE,  
64 linking high boundary layer MSE to high upper-tropospheric potential temperatures (Emanuel and  
65 Bretherton 1994). Within this framework, the impact of a perturbation on the monsoon location  
66 can be understood via its effect on the near-surface thermodynamics. While this theory does not  
67 explain what controls monsoon strength, Harrop et al. (2019) show that the curvature of sub-cloud  
68 moist entropy could be a strong predictor of precipitation minus evaporation. The CQE paradigm  
69 does not seem to hold as cleanly in South America as in other monsoon regions; there is a broad  
70 summer maximum of near-surface moist entropy over the continent, with the maximum upper-  
71 tropospheric saturation moist entropy located near its poleward boundary (Nie et al. 2010). While  
72 useful, the CQE paradigm provides little prognostic power in the absence of a complete theory for  
73 what controls the near-surface MSE distribution itself.

74 Alternatively, some studies use the column-integrated MSE budget as a basis for characterizing  
75 tropical rainfall, including monsoon circulations (e.g. Neelin and Held 1987; Chou and Neelin  
76 2004; Back and Bretherton 2006; Neelin 2007; Hill et al. 2017). The MSE budget, presented in  
77 detail in Section 3b, states that the net column forcing from radiative and turbulent heat fluxes must  
78 balance the atmospheric MSE flux divergence and the time tendency of column-integrated internal

79 energy. While MSE budget analysis is a diagnostic approach, it has been applied in various fruitful  
80 ways, such as: to evaluate the limits on the poleward extent of monsoons (e.g. Chou and Neelin  
81 2001); to identify key mechanisms of tropical precipitation change, such as the “upped-ante” and  
82 “rich-get-richer” responses (Chou and Neelin 2004); and to assess a circulation’s susceptibility to  
83 these responses under climate change (Hill et al. 2017; Smyth and Ming 2020).

84 Unlike the local control of precipitation in the CQE and MSE budget theories, the ITCZ frame-  
85 work takes a unified view of land and ocean precipitation as guided by zonal mean energetics  
86 (Chao and Chen 2001). This perspective is consistent with a global monsoon mode that encom-  
87 passes the solstitial migrations of the convergence zone across the regional subsystems (Geen et al.  
88 2020). As in CQE theory, the view of monsoons as a regional extension of the thermally-direct  
89 Hadley circulation highlights the role of near-surface MSE gradients, rather than temperature gra-  
90 dients, in modulating the monsoon position (Walker et al. 2015). It is also worth noting that the  
91 ITCZ over land and ocean may shift in opposite directions in certain situations, hinting at potential  
92 limitations of the ITCZ framework (Smyth et al. 2018; Hill 2019).

93 It is not straightforward to assess the role of land surface properties within any of the afore-  
94 mentioned monsoon theories. Vegetation impacts both albedo and moisture fluxes, driving feed-  
95 backs between rainfall changes and ecological transitions (Charney 1975). Soil moisture has im-  
96 plications for the partitioning of surface turbulent fluxes, and therefore the surface temperature,  
97 precipitation, and regional circulation (e.g. Seneviratne et al. 2010). In regions with strong land-  
98 atmosphere coupling, including India, West Africa, and parts of tropical South America (Koster  
99 et al. 2004), soil moisture strongly impacts the evaporative fraction and daily maximum surface  
100 temperature (Schwingshackl et al. 2018). Zhou and Xie (2018) utilize an idealized model with  
101 gray radiation to evaluate the role of geometry, albedo, soil moisture, and ocean heat fluxes on  
102 monsoon properties. They find that with the exception of soil moisture, all these factors can be

103 understood via their effects on the surface equivalent potential temperature ( $\theta_e$ , essentially MSE)  
104 distribution, underscoring the importance of CQE dynamics. In their experiments, soil moisture  
105 changes elicit more complex circulation responses that are not always consistent with the migra-  
106 tion of the maximum near-surface MSE, and warrant further study. Zhou and Xie (2018) serves  
107 as a useful comparison point for our results as their model differs only in the lower boundary  
108 condition and their use of a gray radiation scheme.

109 Despite the extensive research highlighted above, fundamental questions persist about the theo-  
110 retical basis of monsoon formation. The complications introduced by zonally confined continental  
111 geometry, land surface moisture constraints, and albedo contrasts have yet to be fully elucidated  
112 (e.g. Zhai and Boos 2015; Maroon and Frierson 2016; Zhou and Xie 2018; Levine and Boos 2017).  
113 The chief purpose of this study is to determine the key mechanisms of monsoon formation across  
114 a broad range of climate conditions. The analysis focuses on the processes driving seasonal pre-  
115 cipitation that would be relevant beyond the idealized model setting. Motivated by a recent work  
116 (Smyth and Ming 2020), we take the summer circulation over South American continental geom-  
117 etry as our focal point, but the analysis aims to elucidate the dynamics of a generic, deep tropical  
118 monsoon. In an idealized framework, the experiments map the parameter space of land albedo and  
119 moisture conditions, with implications for the stages of seasonal monsoon development as well as  
120 the range of global monsoons with their diverse geographic and ecological settings. The holistic  
121 approach draws on numerous relevant theories and suggests some general principles regulating  
122 monsoon strength. Section 2 describes the idealized moist GCM and the suite of experiments.  
123 Section 3a presents the results for varying land moisture conditions, Section 3b is an MSE budget  
124 analysis, and Section 3c examines the land albedo perturbation experiments. Section 4 provides  
125 an overview of the monsoon formation mechanisms over the range of land surface conditions.

## 2. Experimental Design

We use an idealized moist general circulation model as described in Clark et al. (2018). The model has a three dimensional spectral dynamical core, and the highly simplified atmospheric physics largely follows Frierson et al. (2006), including simplified planetary boundary layer and convection schemes. Like Clark et al. (2018), we replace the gray-atmosphere radiation used in Frierson et al. (2006) with a full radiative transfer scheme (Paynter and Ramaswamy 2014). This makes it feasible to explicitly simulate water vapor feedbacks. The simplified Betts-Miller (SBM) convection scheme has a default convective relaxation timescale ( $\tau_{BM}$ ) of 2 hours. This timescale dictates how fast simulated profiles of temperature and humidity are relaxed to convectively adjusted reference states once certain criteria are met (Frierson 2007). The SBM scheme represents shallow, non-precipitating convection by relaxing unstable temperature profiles to reference profiles, and triggers deep, precipitating convection when moisture and temperature profiles exceed stability thresholds, including a 70% relative humidity criterion. Precipitation can also form on the grid scale by removing water vapor in excess of saturation. Neither parameterized convection nor grid-scale precipitation gives rise to clouds. The impact of cloud feedbacks on the monsoon depends on the net radiative effect of the clouds that form (Voigt et al. 2014); this is a source of uncertainty in climate modeling, and is not considered in the present study. While this compromises the realism of the simulations, it allows for a focus on more essential and robust aspects of the monsoon circulations. In Section 4 we compare the results to comprehensive atmospheric model simulations (GFDL AM4.1) that include clouds, topography, and more sophisticated physics, and discuss the relevance of the findings up the model hierarchy.

The lower boundary condition includes a slab mixed layer ocean with a heat capacity equal to 20 meters of water and a prescribed, time-invariant meridional oceanic heat flux, and an isolated



149 South American continent with 10% of the slab ocean heat capacity (i.e. 2 meters of water).  
150 The choice of an isolated continent minimizes the broader climatic impact of land moisture and  
151 albedo perturbations by confining them to a comparatively small area, facilitating comparison  
152 between experiments. On the other hand, the realistic geometry enables more direct comparison  
153 of the monsoon sector with both observations and comprehensive model experiments, including  
154 the Geophysical Fluid Dynamics Laboratory (GFDL) AM4 simulations that motivate the present  
155 study (Smyth and Ming 2020).

156 The South American continent has realistic geometry but no topography (i.e. completely flat),  
157 and does not include Central America. The exclusion of the Andes mountain range is notable given  
158 the attention placed on its climate significance in previous work. For example, the Andes act as a  
159 barrier shielding the continent from low MSE oceanic air (e.g. Garreaud and Aceituno 2001) and  
160 support low level jet formation both by diverting easterly winds and via lee cyclogenesis (Wang  
161 and Fu 2004). We expect the increased ventilation in the absence of the Andes Mountains to limit  
162 the southward extent of the monsoon compared to observations, as in Chou and Neelin (2001).

163 A suite of experiments forced with a modern-day seasonal cycle of insolation is designed to  
164 elucidate the impact of land moisture and albedo conditions on monsoon characteristics. Though  
165 the present study focuses on the case of South America as a bridge to the authors' previous work,  
166 the use of an idealized model and the focus on mechanistic analysis should yield insights that  
167 inform our general understanding of monsoons. The three land moisture configurations include a  
168 "realistic" continent (R) with a bucket hydrology model governing potential evaporation, a "dry"  
169 (D) continent with zero evaporation, and a "wet" continent (W) in which the land is an infinite  
170 reservoir of moisture (i.e. the only distinction between land and ocean is in heat capacity). The  
171 bucket hydrology model (Manabe 1969) in the R configuration scales the potential evaporation  
172 based on a bucket capacity (or field capacity) of 150 mm and a 0.75 saturation fraction, as in

173 Vallis et al. (2018) and Clark et al. (2020). The bucket capacity sets a limit on moisture storage,  
174 and the saturation fraction determines that when the bucket level is below 75% the bucket capac-  
175 ity, the evaporative resistance parameter limits the evaporation to some fraction of the potential  
176 evaporation (see (Vallis et al. 2018)).

177 For each moisture condition, R, D, and W, we perform six albedo perturbation experiments with  
178 land albedo prescribed to 0.1, 0.26, 0.3, 0.4, 0.5, 0.7, and 1.0. Note that 0.26 is the default sur-  
179 face albedo over both land and ocean, and is chosen to attain a realistic climate in the absence of  
180 clouds (Frierson et al. 2006). The name of an experiment contains a letter (denoting the moisture  
181 condition) followed by a number (denoting the albedo). For instance, R0.26 refers to the experi-  
182 ment in which one uses the bucket hydrology model and the default albedo of 0.26. To discern the  
183 effect of the convective relaxation time on the monsoon simulation, we examine three experiments  
184 in the R0.26 configuration with  $\tau_{BM}$  varied to 4, 8, and 16 hours, as in Clark et al. (2018). The  
185 CO<sub>2</sub> concentration is prescribed to 369.4 ppm, and CH<sub>4</sub> to 1.821 ppm. The experiments are run  
186 at T42 spectral resolution (64 latitude by 128 longitude gridpoints) with 30 vertical levels. Each  
187 simulation is run for 20 years with the final 15 years of daily output used for analysis.

### 188 3. Results

#### 189 *a. Varying land moisture conditions*

190 Irrespective of the local moisture availability in the idealized model simulations, the seasonal  
191 cycle over the South American monsoon sector (5-18° S, 40-72° W) is distinctly monsoonal in  
192 all three experiments with the default surface albedo (0.26) (Fig. 1a). Modest precipitation com-  
193 mences in October, two to three months after surface temperatures ( $T_{surf}$ ) shift to a warming  
194 trajectory in late winter (Fig. 1b). With bucket hydrology (R0.26), a maximum rainfall rate of

195 6.2 mm d<sup>-1</sup> occurs in February, and without a local moisture source (D0.26), the peak monthly  
 196 mean rainfall of 4.4 mm d<sup>-1</sup> occurs a month earlier, in January. When local moisture is unlimited  
 197 (W0.26), rainfall maximizes at 9.1 mm d<sup>-1</sup> in February. [Throughout the paper, the monsoon  
 198 season refers to January to March (JFM), the period encompassing the highest mean rainfall rate.]  
 199 In R0.26,  $T_{surf}$  decreases as precipitation intensifies in JFM because in a moisture-limited regime,  
 200 latent heat fluxes can increase at the expense of sensible heat fluxes (e.g. Berg et al. 2015). In  
 201 D0.26 and W0.26, this coupling is eliminated since the local moisture is externally controlled.  
 202 This may partly explain why  $T_{surf}$  in the dry and wet cases is relatively flat during the monsoon  
 203 season. In all experiments, precipitation rapidly retreats from April through June, and the dry sea-  
 204 son extends from July through September (JAS). During this time, there is virtually zero rainfall  
 205 when local moisture fluxes are limited or disabled, while the mean precipitation hovers around 1  
 206 mm d<sup>-1</sup> in the W0.26 experiment (Fig. 1a). Insolation minimizes in June, and minimum surface  
 207 temperatures lag this by one month in the R0.26 and D0.26 experiments and by two months in  
 208 W0.26 (Fig. 1b). In D0.26, surface temperatures respond more strongly to the insolation forcing  
 209 without the moderating effect of latent heat fluxes on the surface energy balance. The D0.26 exper-  
 210 iment exhibits the lowest amplitude annual cycle of precipitation, but the most seasonal variation  
 211 of surface temperature (13 K range, compared to 11 K in R0.26 and 8 K in W0.26).

212 From a net precipitation perspective ( $P - E$ ) (equivalent to the large-scale moisture conver-  
 213 gence), the rainy season disparity between experiments is smaller, given the substantial enhance-  
 214 ment of evaporation in the R and W experiments (Fig. 1c). Note that there is no land evaporation  
 215 in the D experiment, so  $P - E$  is the same as  $P$ . The JFM mean  $P - E$  is similar in D0.26 (4.2 mm  
 216 d<sup>-1</sup>) and W0.26 (3.1 mm d<sup>-1</sup>), which underscores the prominent role of the large-scale circulation  
 217 in importing moisture from the ocean in both extreme cases. The  $P - E$  is lower in R0.26 (1.8 mm  
 218 d<sup>-1</sup>); moisture convergence is higher with dry or saturated land than with bucket hydrology. Dur-

219 ing the dry season, the disparity in  $P - E$  is greater than that in precipitation; the JAS mean  $P - E$   
 220 is negative in R0.26 ( $-0.33 \text{ mm d}^{-1}$ ) and W0.26 ( $-2.6 \text{ mm d}^{-1}$ ). In W0.26,  $P - E$  remains negative  
 221 into the monsoon onset season (October through December, or OND) before increasing sharply. In  
 222 the W0.26 simulation this continental region serves as a prominent net moisture source for much  
 223 of the year, an unrealistic consequence of simulating land without a limit on potential evapora-  
 224 tion. Nonetheless, the magnitude and phasing of the precipitation in W0.26 is remarkably similar  
 225 to the observed 1997-2015 annual cycle from the Global Precipitation Climatology Project v2.3,  
 226 especially from January to August (Fig. 1a). In this model, a saturated land surface produces the  
 227 most realistic seasonal cycle of precipitation over the monsoon sector in terms of magnitude and  
 228 timing; perhaps the saturated land best represents the strong evapotranspiration from vegetation  
 229 in this region. In all three idealized model experiments the monsoon onset season precipitation is  
 230 delayed and substantially weaker than observed, underlying a rather abrupt transition.

231 Despite the simplicity of the model configuration, especially in the absence of the Andes Moun-  
 232 tains, the spatial distribution of monsoonal precipitation is largely consistent with observed pat-  
 233 terns (Fig. 2), suggesting that the realistic geometry and the differing heat capacity of land and  
 234 ocean are sufficient to induce a fairly realistic monsoonal climate in the presence of insolation  
 235 forcing. The key discrepancy in the atmospheric circulation without the Andes is that low-level  
 236 westerly flow from the tropical Pacific contributes to the continental moisture convergence (Fig.  
 237 3). This westerly inflow is particularly strong in D0.26, where a cyclonic circulation on the west-  
 238 ern continent (Fig. 3a) produces a precipitation maximum near  $70^\circ \text{ W}$ , with a relatively narrow  
 239 rainfall band extending across the width of the monsoon sector (Fig. 2a). Precipitation exceeding  
 240  $4 \text{ mm d}^{-1}$  extends from the east coast to  $60^\circ \text{ W}$  in R0.26, with the strongest mean precipitation  
 241 near  $40^\circ \text{ W}$  (Fig. 2b). When surface moisture is unlimited, the monsoon is coherent with the

oceanic Intertropical Convergence Zone (ITCZ) both west and east of the continent, though the precipitation has a broader southward extent over South America (Figs. 2c, 5c).

One notable feature in the simulations is the limited southeastward extension of the South Atlantic Convergence Zone (SACZ), a convective band that emanates from the Amazon basin over the South Atlantic Ocean. Previous work suggests that the SACZ forms when midlatitude fronts stall at longitudes with enhanced tropical convection and Rossby waves propagate equatorward (Nieto Ferreira and Chao 2013; Van Der Wiel et al. 2015). In a series of aquaplanet experiments, Nieto Ferreira and Chao (2013) find that an SACZ-like feature develops when a prescribed patch of enhanced tropical convection attains sufficient strength and poleward extent. In line with Kodama (1992, 1993), they emphasize that strong poleward low-level flow on the eastern flank of the monsoon region, or along the west of the subtropical high, is crucial for moisture convergence and SACZ formation. The underdevelopment of the SACZ may be attributed to discrepancies in the location and intensity of such a low-level jet in the idealized simulations. In all three experiments, poleward flow on the eastern coast of the continent does not extend poleward of  $15^{\circ}\text{S}$  (Fig. 3). In R0.26 and W0.26, the winds have a northwesterly orientation and are relatively weak, possibly due to the weaker land-ocean thermal gradients.

Like the magnitude of the precipitation, the region-mean near-surface (973 hPa) JFM MSE increases with local moisture availability. The MSE or  $h$  is defined as  $h = c_p T + gz + L_v q - L_f q_{ice}$ , where  $c_p$  is the heat capacity of air at constant pressure,  $T$  is temperature,  $g$  is the gravitational constant,  $z$  is geopotential height,  $L_v$  is the latent heat of vaporization of water, and  $q$  is specific humidity. In D0.26, the near-surface MSE is lower over the central monsoon sector than the surrounding coastal land, which is mirrored by the precipitation distribution (Fig. 2a). The MSE distribution is more uniform over land and ocean in R0.26 and W0.26 (Fig. 2b, c). In R0.26 the highest near-surface MSE contour bisects the maximum precipitation, and in W0.26, the near-

surface MSE is highest just poleward of the strongest precipitation, consistent with CQE theory (Emanuel 1995; Privé and Plumb 2007a; Nie et al. 2010). In Section 3c we examine the extent to which the MSE distribution guides the precipitation when land albedo is varied (Hurley and Boos 2013).

While each of these baseline experiments exhibits a monsoonal climate, the precipitation originates via different pathways in the model. With dry land, all moisture for precipitation derives from oceanic regions, so the monsoon sector is particularly reliant on easterly and westerly inflow of moist air from the tropical ocean. With unlimited moisture, the mean JFM evaporation rate is 60% of the precipitation rate, which points to the substantial local moisture recycling evident from the  $P - E$  results. Additionally, in D0.26, the rainy season precipitation ( $4.2 \text{ mm d}^{-1}$ ) derives almost exclusively from large-scale processes, with precipitation occurring when an entire grid box reaches saturation (not shown). By contrast, in the R0.26 ( $5.3 \text{ mm d}^{-1}$ ) and W0.26 ( $7.8 \text{ mm d}^{-1}$ ) experiments, JFM precipitation is largely produced by the parameterized Betts-Miller convection scheme (88% and 96%, respectively). Given the 70% relative humidity threshold in the SBM convection scheme, the ratio of convective to large-scale strongly depends on the near-surface humidity (Frierson 2007), a point to which we will return.

The underlying large-scale circulation characteristics differ markedly across the range of land moisture conditions. The monsoon-sector mean ascent profiles in the R0.26 and W0.26 experiments indicate top-heavy moist convection that penetrates the upper troposphere, with vertical velocity maxima ( $50$  and  $70 \text{ hPa d}^{-1}$ , respectively) at approximately  $400 \text{ hPa}$  (Fig. 4a). The dry land case is characteristic of a shallow overturning circulation with vigorous ascent; the maximum vertical pressure velocity ( $\omega$ ) is  $120 \text{ hPa d}^{-1}$  at  $750 \text{ hPa}$  (Fig. 4a). Though the ascent profile is relatively shallow, weaker ascent does penetrate to  $250 \text{ hPa}$ .

289 The region-mean MSE profiles also reflect the differing nature of the monsoon across moisture  
290 conditions (Fig. 4b). Although MSE decreases with height in the lower troposphere in all cases be-  
291 fore starting to increase, the location of the MSE minimum becomes progressively lower in height  
292 with the increasing availability of moisture. Note that the observed tropical MSE profile typically  
293 shows a minimum in the mid-troposphere (around 600 hPa) (Back and Bretherton 2006). A possi-  
294 ble reason is that the free troposphere in the idealized simulations is biased dry, presumably due to  
295 the absence of moistening through convective detrainment of cloud condensates. The comparably  
296 low near-surface MSE in D0.26 demonstrates the strong effect of local moisture limitations on the  
297 overlying atmosphere.

298 The R0.26 and W0.26 profiles are firmly under convective quasi-equilibrium (CQE) control,  
299 with precipitation produced primarily via the simplified Betts-Miller (SBM) convection scheme.  
300 It seems questionable whether this is the case for D0.26, in which the parameterized convection  
301 ceases to operate and precipitation is produced exclusively through large-scale processes. How-  
302 ever, the resolved (grid-scale) convection, albeit pathological, may still play a role in establishing  
303 a linkage between near-surface and upper-tropospheric MSE.

304 It is interesting to think about what controls the upper-tropospheric MSE in these experiments.  
305 CQE states the expectation that in convecting regions, one should see covariation of boundary  
306 layer equivalent potential temperature and the upper-tropospheric saturation value (e.g. Nie et al.  
307 2010). The free tropospheric saturation value depends on temperature only, so maxima in bound-  
308 ary layer  $\theta_e$  should correspond to overlying maxima in free-tropospheric temperature. In the weak  
309 temperature gradient (WTG)/CQE framework (e.g. Byrne and O’Gorman 2013; Hill et al. 2017;  
310 Zhang and Fueglistaler 2020), the upper-tropospheric MSE throughout the inner tropics is dictated  
311 by the highest near-surface MSE. Fig. 5 shows that the highest near-surface MSE is located over  
312 the land monsoon region and the adjacent ocean in R0.26 and W0.26. In both cases, the upper

313 tropospheric temperatures are fairly uniform, varying by less than 3-K in the inner tropics, as ex-  
314 pected due to WTG dynamics (Fig. S1). The warmest temperatures extend over the monsoonal  
315 precipitation and near-surface MSE maxima, in accordance with the CQE framework. In D0.26,  
316 the maximum MSE is west of the land precipitation maximum, outside the high-precipitation con-  
317 tours where convection would convey this MSE maximum to the upper-troposphere. The D0.26  
318 experiment stands out in that the upper-tropospheric temperature is lowest over the monsoon sec-  
319 tor, directly above the local precipitation maximum. The bottom-heavy convection indeed leads  
320 to some deviation from CQE conditions over dry land (Fig. 4a). Despite this, continental precipi-  
321 tation in D0.26 appears near the near-surface MSE maximum along the western continental coast  
322 (Fig. 5).

323 The impact of varying land moisture availability is also evident in the vertical distributions  
324 of several other key variables. The dry static energy (DSE) profiles reflect hotter near-surface  
325 conditions in the D0.26 experiment as well as a much deeper boundary layer in which quasi-  
326 conserved quantities such as DSE are relatively well-mixed (Fig. 4c). This homogenization occurs  
327 partly via non-precipitating (dry), shallow convection in the SBM convection scheme (Frierson  
328 2007). Near-surface DSE is highest in the D0.26 experiment and lowest in the W0.26 experiment.  
329 By contrast, in the upper troposphere, DSE is highest in the W0.26 experiment and lowest in  
330 the D0.26 experiment. As this part of the atmosphere is devoid of moisture (i.e. similar DSE  
331 and MSE), it means that the increased availability of land moisture leads to a warming of the  
332 upper troposphere. This is a manifestation of the relative standing in near-surface MSE across the  
333 experiments which impacts the upper troposphere through convection.

334 The vertical distribution of specific humidity ( $q$ ) also varies in these experiments. D0.26 has a  
335 much drier boundary layer than R0.26 and W0.26. In all cases, relatively high near-surface mois-  
336 ture values fall off sharply with height at least partly owing to the missing convective detrainment,



reducing tropospheric relative humidity values (Fig. 4d,e). Consistent with these temperature and moisture distributions, the D0.26 experiment has arid near-surface conditions with 25% mean relative humidity (RH) compared to 60% and 70% RH in the R0.26 and W0.26 experiments, respectively (Fig. 4e), which are sufficiently close to the SBM convective threshold (70%). By contrast, it is far too dry for convective precipitation in D0.26. The precipitation intensity distributions also reflect this; in W0.26 the daily rainfall distribution is spread broadly over the 0 to 20 mm d<sup>-1</sup> range due to frequent moist convection (not shown). In D0.26 by contrast, the distribution has a long tail of infrequent extreme rain events (produced by large-scale scheme), while on the majority of days there is near-zero rainfall.

#### b. MSE Budget Analysis

The region-mean MSE budget analysis further illustrates the differing character of the monsoonal circulation in the experiments. The column-integrated MSE budget is given by:

$$\frac{\partial}{\partial t}\{\overline{\mathcal{E}}\} + \{\bar{\mathbf{v}} \cdot \nabla_p \bar{h}\} + \left\{ \bar{\omega} \frac{\partial \bar{h}}{\partial p} \right\} + \nabla \cdot \{\overline{h' \mathbf{v}'}\} \approx \bar{F}_{net}, \quad (1)$$

wherein brackets denote mass-weighted column integrals, overbars are time means, primes are temporal deviations,  $\mathcal{E}$  is the internal plus potential energy,  $\mathbf{v}$  is the horizontal wind vector,  $\nabla_p$  is the horizontal gradient operator on constant pressure surfaces,  $\omega$  is vertical velocity in pressure coordinates, and  $\bar{F}_{net}$  is the net column energy.  $\bar{F}_{net}$  is the sum of top-of-atmosphere (TOA) and surface radiative fluxes into the column plus the surface turbulent fluxes.

Based on a calculation of the region mean column-integrated MSE budget (Table 1) following Hill et al. (2017), the vertical MSE advection is negative in the D0.26 experiment, denoting energy import by the circulation, and positive in the R0.26 and W0.26 experiments. In all three cases, the DSE component of the vertical MSE advection term is positive, since DSE increases with altitude,

while the moisture component is negative. Only in the D0.26 experiment does the latter dominate. Between 600 and 800 hPa the vertical moisture gradient, decreasing with altitude, is sampled by very strong vertical velocity values.

The negative  $\left\{ \overline{\omega} \frac{\partial \bar{h}}{\partial p} \right\}$  in D0.26 corresponds to a negative gross moist stability (GMS). The GMS relates the column energy transport to the strength of the mean circulation and can be thought of as the efficiency of a circulation's energy export (Bretherton et al. 2006). It is determined by the structure and amplitude of the vertical velocity, along with the stratification of the MSE. In this sense, the D0.26 monsoon circulation is similar in nature to the observed East Pacific ITCZ, a region of relatively shallow precipitating convection with a negative GMS (Back and Bretherton 2006). By contrast, the monsoon dynamics in R0.26 and W0.26 resemble the deep convection of the West Pacific ITCZ, with positive vertical MSE advection values denoting energy export. These circulations comply with the Neelin and Held (1987) theory of tropical rainfall in which vertical MSE advection plays a chief role in balancing column heating, and precipitating tropical convection is associated with a positive GMS.

The horizontal MSE advection term is similar across the three experiments, between 5 and 10  $\text{W m}^{-2}$ , and contributes to MSE export in each case. A decomposition of the horizontal MSE advection into dry and moist components, however, reflects differences between the experiments. In D0.26, the advection of relatively cool, moist air from the adjacent ocean produces a positive horizontal DSE advection ( $\{\bar{\mathbf{v}} \cdot \nabla_p \overline{DSE}\} = 39.2 \text{ W m}^{-2}$ ) and a negative column horizontal moisture advection ( $\{\bar{\mathbf{v}} \cdot \nabla_p \overline{L_v q}\} = -33.7 \text{ W m}^{-2}$ ). In the R0.26 and W0.26 configurations, the region mean horizontal DSE advection is near zero (2.4 and -0.1  $\text{W m}^{-2}$ ), while the horizontal moisture advection is positive, denoting export (7.8 and 6.4  $\text{W m}^{-2}$ ). These results indicate a relatively small land-sea temperature contrast and higher specific humidity over land than over ocean.  $F_{net}$  differs by an order of magnitude between the experiments, ranging from 7.8  $\text{W m}^{-2}$  in D0.26 to 64

382  $\text{W m}^{-2}$  in W0.26. This is due primarily to differences in outgoing longwave radiation (OLR), with  
383 higher surface temperatures and thus OLR over dry land. The impact of the net column energy flux  
384 on the regional climate is examined further in the analysis of the albedo perturbation experiments.

385 The budget analysis demonstrates that in all three baseline experiments, precipitation is gener-  
386 ated by the mean flow rather than transients. Mean ascent in the monsoon sector drives moisture  
387 convergence and precipitation, while transient eddies diverge moisture. The eddy MSE flux di-  
388 vergence is dominated by the moisture contribution in all three experiments, and the DSE com-  
389 ponent is negative in R0.26 and W0.26, indicating DSE convergence over the monsoon sector.  
390 The predominance of the mean circulation in generating precipitation is further supported by an  
391 assessment of the JFM mean potential vorticity (PV) distribution over continental longitudes (not  
392 shown). A necessary condition for baroclinic instability is a reversal of the meridional PV gradi-  
393 ent (Charney and Stern 1962; Hsieh and Cook 2005), and this is not satisfied in D0.26 or W0.26.  
394 In R0.26, a PV gradient reversal at 600 hPa along the southern margin of the monsoon sector  
395 suggests a possible role for baroclinic instability. Rayleigh’s criterion for barotropic instability (a  
396 change in sign of  $\beta - u_{yy}$ ) is not satisfied in any of the three baseline experiments (not shown).

### 397 *c. Land albedo perturbation experiments*

398 To better understand the impact of net column energy fluxes on monsoon characteristics, as  
399 well as the limits of monsoonal climate regimes, we examine a suite of land albedo perturbation  
400 experiments. Land albedo variations drastically impact the monsoonal precipitation magnitude  
401 (Fig. 6), in agreement with previous studies (Zhou and Xie 2018; Boos and Storelvmo 2016).  
402 With all three moisture conditions, JFM precipitation declines monotonically with increasing land  
403 albedo, with minimal rainfall at albedo values of 0.5 or higher. Regardless of local moisture

availability, when the albedo is increased to 0.7 or 1.0, the monsoon region is subject to mean descent throughout the atmospheric column (Fig. 7).

The surface temperatures over land in the R0.5 and D0.5 experiments (296 K and 301 K, respectively) remain higher than adjacent SSTs, so that a weak, viscously driven circulation persists, though it produces negligible precipitation (Fig. 7a, b; Fig. 6). In the R and D experimental suites, ascent is confined to the boundary layer when albedo values are prescribed to 0.4 or 0.5 (Fig. 7a,b). In these simulations, the surface temperature distributions induce low-level pressure gradients which drive convergence over the monsoon sector. In the lower range of land albedo values, the R and D experiments diverge. In the D0.3, D0.26, and D0.1 experiments, the ascent grows increasingly vigorous and vertically extended. While the ascent maximum is relatively low in each of these experiments (below 650 hPa), the ascending motion extends through the mid-troposphere, and is accompanied by a jump in precipitation intensity with mean values of 3.4, 4.2, and 6.9 mm d<sup>-1</sup>, respectively, compared to 1.3 mm d<sup>-1</sup> in the D0.4 experiment (Fig. 6). Even when land albedo is lowered to 0.1 in the dry land configuration, the precipitation derives almost exclusively from the large-scale scheme. By contrast, in the R0.3, R0.26, and R0.1 experiments, deep convection develops and precipitation increases to 3.7, 5.3, and 9.1 mm d<sup>-1</sup>, respectively. The shape of the ascent profiles and the proportion of convective to total precipitation support that convective instability underlies the monsoon development in these R experiments.

In the wet land configuration, land albedo variations do not alter the precipitation mode; in any experiment in which land remains thermodynamically favorable, precipitation is driven almost exclusively by convective instability. In W0.1 the vertical velocity profile strengthens, and when the land albedo is increased to 0.3 or 0.4, convection weakens but remains vertically extensive (Fig. 7c). In the W0.5 experiment, without land-ocean gradients in surface moisture availability, the albedo perturbation reduces the temperature of land to 290 K, below that of the nearby sea

428 surface, resulting in mean descent through the column (Fig. 7c). Boundary-layer confined ascent  
429 only develops in the simulations with land moisture limitations.

430 We consider the hypothesis that inertial instability underlies the enhancement of the monsoonal  
431 circulation in the three dry low-albedo experiments (i.e. D0.3, D0.26, and D0.1) (Plumb and Hou  
432 1992; Tomas and Webster 1997). The near-surface (920 hPa) absolute vorticity ( $\eta$ ) distribution  
433 supports this, as the zone of locally anticyclonic absolute vorticity expands with the off-equatorial  
434 migration of the  $\eta = 0$  contour over continental latitudes when albedo is reduced below 0.4 (Fig.  
435 8a, b). In inertially unstable zones, the divergent wind accelerates to generate a locally cyclonic  
436 tendency term, relaxing the instability. The resulting convergence zone intensifies local convec-  
437 tion and precipitation. In the three low-albedo experiments, the near-surface divergence over the  
438 central continent is predominantly equatorward of  $\eta = 0$ , with the convergence zone largely lying  
439 poleward thereof, consistent with Tomas and Webster (1997) (Fig. 8a, b). This is not the case  
440 in the higher albedo experiments, including D0.4 and D0.5, in which the continental convergence  
441 zone straddles the  $\eta = 0$  contour which hovers closer to the equator (Fig. 8c, d). Furthermore,  
442 the highest 920 hPa divergent wind speeds are bisected by the  $\eta = 0$  contour when it deviates  
443 poleward over the continent in the D0.3, D0.26, and D0.1 experiments (Fig. S5). In D0.4 and  
444 D0.5, the maximum divergent wind speeds over continental longitudes occur north of the equator  
445 (Fig. S5).

446 In the R and W experimental suites, inertial instability seems to play a less central role in mon-  
447 soon development. In February, the  $\eta = 0$  contour migrates only slightly further poleward over  
448 the continent than over the adjacent ocean, and the displacement is smaller than in the dry land  
449 experiments (not shown). For example, in D0.26, the maximum southward displacement of the  
450 contour over the continent is  $4.2^\circ$ , compared to  $2.4^\circ$  in the R0.26 experiment and  $2.7^\circ$  in W0.26.

451 This disparity may be explained by the relatively strong cross-equatorial pressure gradient in the  
452 dry land experiments caused by the particularly strong heating of the continent.

453 In terms of the spatial distribution of precipitation, the effect of albedo variations depends on  
454 the land moisture configurations (Figs. S2-S4). In the D configuration, the near-surface MSE  
455 maximum does not shift substantially in response to albedo perturbations. Correspondingly, there  
456 is little latitudinal change in the monsoon location. At lower albedo values in the W configuration,  
457 and to a lesser extent in R, the near-surface MSE maximum increases and shifts poleward, and  
458 the monsoon expands poleward, in accordance with CQE predictions (Hurley and Boos 2013).  
459 In both the R and W experiments, JFM precipitation is strongest near the Atlantic coast, and  
460 as the continent heats up at lower albedo values, the monsoon penetrates further westward over  
461 the continent. Increased continental heating and thermal gradients can enhance baroclinicity of  
462 prevailing easterlies and thus convective storm formation, driving a westward expansion of the  
463 monsoon; such a process underlies the strengthening of African Easterly Wave activity in global  
464 warming simulations (Skinner and Diffenbaugh 2014). The spatial pattern of precipitation differs  
465 in the D suite; a local precipitation maximum near the west coast, coinciding with a local MSE  
466 maximum, emerges when the land albedo is 0.3 or lower (Fig. 5). The thermal low over the  
467 continent induces convergence of westerly winds from the Pacific and easterly winds from the  
468 Atlantic. These lower-tropospheric winds are stronger in the D suite than the corresponding R  
469 and W experiments due to the relatively strong land-sea thermal contrast (Fig. 3). With realistic  
470 topography, this moist westerly inflow would be impeded by the Andes.

471 When land surface albedo is varied across a broad range, various types of monsoonal circula-  
472 tions arise. At the highest albedo values, the land surface is cooler than the zonal mean value and  
473 the monsoon vanishes. At moderate albedo values, a viscously driven circulation emerges in local  
474 summer, producing a modest seasonal cycle of precipitation over off-equatorial South America.

475 When albedo is reduced to 0.4 or below, inertial instability triggers enhanced convergence and  
 476 precipitation in the dry land experiments, while convective instability produces more substantial  
 477 rainfall in the realistic and wet land configurations. Even when the land albedo is suppressed  
 478 to 0.1, the absence of latent heat fluxes leads to an exceedingly dry boundary layer and inhibits  
 479 parameterized moist convection in the dry land experiment. It is notable that even without trig-  
 480 gering parameterized convection, the JFM precipitation in D0.1 is substantial ( $6.9 \text{ mm d}^{-1}$ ) and  
 481 exceeded only by the W0.26, W0.1, and R0.1 experiments ( $7.8, 12.2, 9.1 \text{ mm d}^{-1}$ , respectively).  
 482 When  $F_{net}$  is sufficiently strong due to the sensible heat flux, moisture transport and convergence  
 483 partially compensate for the disabling of local moisture recycling. Evidently, while a local mois-  
 484 ture limitation shapes the monsoonal regime, this parameter alone does not impede the monsoon's  
 485 emergence nor its intensification. This has implications for monsoon onset, which occurs when  
 486 local moisture availability is constrained following the dry season in South America. Throughout  
 487 the spring, increasing local soil moisture and latent heat fluxes enable the vigorous convection of  
 488 the monsoon season (Fu and Li 2004). The processes driving the initial precipitation that primes  
 489 the region for monsoon development may resemble the mechanisms in the D suite (i.e. inertial  
 490 instability).

491 Regardless of the physics underlying precipitation development across the suite of experiments,  
 492 the JFM precipitation increases nearly linearly with  $F_{net}$ , suggesting that this is a key parameter  
 493 modulating monsoon intensity (Fig. 9a). Moderate precipitation develops only when  $F_{net}$  values  
 494 exceed zero. While local moisture conditions circumscribe the physical triggers of convection, in  
 495 any case the magnitude of the precipitation is related to the magnitude of the MSE flux divergence.  
 496 The circulation must comply with the MSE budget, meaning the MSE flux divergence by the to-  
 497 tal circulation (horizontal advection, vertical advection and eddies) must balance the net forcing  
 498 and the time tendency (the latter changes negligibly). A higher net column forcing necessitates a

stronger mean circulation and/or more pronounced MSE gradients on which the circulation acts. In the dry land experimental suite, the circulation strength (using vertical pressure velocity as a proxy) increases drastically as albedo is reduced, supporting more moisture import and stronger convergence (Fig. 7a). In the experiments with higher land moisture availability, the circulation strength also increases with the net column forcing, albeit more modestly. In each suite of experiments, there is a concomitant enhancement of precipitation. This relationship between precipitation and net column forcing aligns with the findings of Boos and Storelvmo (2016), who demonstrate that monsoon strength has a nearly linear dependence on radiative forcing in both a comprehensive GCM and an analytical model.

Examining the TOA components of the net forcing term, the relationship between precipitation and net shortwave radiation is more consistent among experiments than the relationship between precipitation and OLR (not shown). As described earlier, the OLR is consistently higher in the dry land experiments due to the restrictions imposed on the land surface energy budget. By the same reasoning, the region-mean OLR at a given precipitation rate is consistently lower in the wet land experiments than the R experiments.

To better compare thermodynamic conditions given these moisture-modulated differences in the surface energy budget, we examine the relationship between near-surface  $\theta_e$  and precipitation. In all three configurations, as albedo decreases, precipitation increases accompany increases in both the continental near-surface  $\theta_e$  and its horizontal gradient (Fig. 9b, c). This underscores that a positive relationship between the amplitude of precipitation and near-surface  $\theta_e$  can persist even when parameterized convection is largely inactive (Fig. 9b). Figure 9b illustrates a threshold behavior: all experiments with region-mean  $\theta_e$  below 302 K have negligible precipitation. In the remaining experiments, in which region-mean  $\theta_e$  values range from 306 K to 313 K, precipitation steadily increases with  $\theta_e$  regardless of the land moisture condition. Fig (9c) is relevant for understanding



523 this threshold behavior: the onset of appreciable monsoonal precipitation occurs when the mon-  
524 soon sector region-mean near-surface MSE approaches or exceeds the tropical mean value. It is  
525 striking that this relationship holds in the dry land experiments, given the impedance of parame-  
526 terized convection, the shallow ascent profile (Fig. 4a), and the disruption of CQE conditions in  
527 the atmosphere (Fig. S1), as in Zhou and Xie (2018).

## 528 4. Discussion

529 The suite of idealized model experiments demonstrates the profound impact of land surface con-  
530 ditions on monsoon dynamics. These experiments, and the precipitation mechanisms they reveal,  
531 may inform our understanding of the stages of monsoon development on Earth. As an example,  
532 we consider the seasonal cycle over the South American monsoon sector as simulated in the GFDL  
533 AM4 model with prescribed climatological SSTs. In previous work, the authors examined the sea-  
534 sonally varying responses of precipitation in the South American monsoon sector to uniform 2-K  
535 SST warming in the GFDL AM4 model (Smyth and Ming 2020). Though the spring and fall are  
536 both characterized by moderate precipitation rates and similar region-mean MSE budget regimes  
537 in AM4, they exhibit different responses to warming. Spring rainfall decreases by 11% and  $P - E$   
538 decreases by 40%, while fall rainfall remains unchanged. This difference is linked to the difference  
539 in the climatological low-level relative humidity, which is 60% in spring and 80% in fall. The  
540 seasonal contrast in RH impacts the surface temperature and boundary layer MSE distributions  
541 and leads to different anomalous patterns in the SST warming experiment. Ultimately, the more  
542 pronounced land-sea contrast in spring renders the season vulnerable to drying by anomalous hor-  
543 izontal MSE advection in the +2-K experiment. The study concludes that differing boundary layer  
544 humidity plays a crucial role in setting the monsoon properties and thus the sensitivity to perturba-  
545 tions. This echoes Byrne and O’Gorman (2015), who find that changes in the horizontal gradients

546 of temperature and fractional changes in relative humidity explain why the  $P - E$  response over  
547 land deviates from the canonical wet-get-wetter scaling. To what extent can the idealized model  
548 results shed light on these findings?

549 To assess whether the linear relationship between net column heating and precipitation holds  
550 beyond the idealized modeling framework, Figure 9a includes the data points for the four seasons  
551 in AM4 control and +2-K experiments. The seasonal cycle in AM4 exhibits hysteresis in this  
552 parameter space (Fig. 9a). In SON, preceding the rainy season, the AM4 control net column  
553 heating is  $69.5 \text{ W m}^{-2}$  and the precipitation rate is  $4.1 \text{ mm d}^{-1}$ . Following the rainy season, in  
554 MAM, the net column heating is lower ( $42.5 \text{ W m}^{-2}$ ) while the precipitation rate is higher ( $6.9$   
555  $\text{mm d}^{-1}$ ). As noted above, the shoulder seasons have similar MSE budget regulation regimes, as  
556 characterized by the relative strength of vertical to horizontal MSE advection (Smyth and Ming  
557 2020). Mapping the seasonal cycle in Figure 9a points to the impact of the differing surface  
558 moisture availability on the efficiency of precipitation production. SON exhibits a clear deviation  
559 from the largely linear relationship across the idealized experiments and the other AM4 seasons  
560 (Fig. 9a). Based on net column heating, AM4 SON is most similar to W0.26 ( $F_{net} = 64.3 \text{ W m}^{-2}$ ),  
561 but the W0.26 rainfall is nearly twice as strong ( $7.84 \text{ mm d}^{-1}$ ). When land surface moisture is  
562 limited, substantial moisture convergence from the ocean is needed to produce rainfall. In SON,  
563 the land heating is less pronounced than in the D suite and the circulation is substantially weaker,  
564 while the dry soil remains a limiting factor in generating precipitation.

565 The idealized experiments also exhibit seasonal hysteresis in the relationship between  $F_{net}$  and  
566 precipitation, despite the fact that land surface moisture is externally controlled in D0.26 and  
567 W0.26. The seasonal cycle for D0.26 resembles that in AM4, though with reduced seasonal vari-  
568 ability along both axes (Fig. 9a). This implies that the asymmetry between monsoon onset and  
569 withdrawal is due to the nature of the circulation, and is not entirely a consequence of season-

ally varying land surface moisture availability or cloud radiative effects. Though  $F_{net}$  decreases strongly from summer to fall, even dropping below zero in D0.26, the circulation persists and continues to support relatively high precipitation rates. Monsoon withdrawal follows an equatorward and off-continental shift of near-surface MSE and temperature maxima (not shown). Figure 9b includes data for all four seasons of the D0.26, R0.26, and W0.26 experiments, and demonstrates a consistent relationship between near-surface  $\theta_e$  and precipitation throughout the seasonal cycle. The near-surface MSE is consistently higher in the comprehensive GCM AM4, but the direct relationship between near-surface MSE and precipitation intensity holds throughout the seasonal cycle (Fig. 9b). While the net column heating varies directly with the strength of the summer monsoonal circulation, the near-surface  $\theta_e$  is a better guide for capturing the monsoon-sector precipitation variability across seasons in both the idealized and comprehensive models. The near-surface  $\theta_e$  contrast between the monsoon sector and the tropical mean also regulates the intensity of monsoon-sector precipitation throughout the seasonal cycle in the idealized experiments (Fig. 9c). As for the JFM data, substantial precipitation only occurs as the monsoon sector thermodynamic state approaches the tropical mean value. The strong relationships between precipitation and  $\theta_e$  or contrasts thereof hold even in the dry land suite, when CQE conditions are not strictly satisfied. In AM4, the spring and fall deviate from the idealized model results, while the summer and winter values are remarkably consistent with the idealized model results (Fig. 9c).

The discrepancy between the monsoon onset season in AM4 (SON) and the idealized experiments is likely linked to the absence of one or more key processes from the idealized configuration. Connections between the idealized model simulations and AM4, or reality, must be drawn cautiously given the drastic simplification of the climate in the idealized experiments. The absence of global continental geometry impacts the general circulation in the idealized experiments, and much of the physics is greatly simplified. In particular, the effects of clouds on surface tempera-

ture, radiative fluxes (and thus  $F_{net}$ ), and precipitation generation are noteworthy. Clouds might, for example, reduce surface temperatures over land and impede circulation strength in AM4 SON as compared to the idealized simulations with limited land moisture (eg. Sharma et al. 1998).

The conclusions are largely robust to variations in the convective relaxation timescale, except that the ratio of large-scale to convective rainfall depends strongly on this parameter. In the R0.26  $\tau_{BM}$  experiments, the percentage of precipitation deriving from the SBM scheme is 88% in the control ( $\tau_{BM} = 2$  h), 81% with  $\tau_{BM} = 4$  h, 71% with  $\tau_{BM} = 8$  h, and only 36% when  $\tau_{BM} = 16$  h. As expected, the near-surface relative humidity increases with the relaxation time, since the moisture profiles are less frequently relaxed via the convection scheme. The climate is otherwise robust to  $\tau_{BM}$ , which has no notable impact on the total precipitation, nor on the region-mean surface temperature, OLR, net column energy flux, or moisture convergence ( $P - E$ ).

Figure 10 provides a schematic overview of the monsoonal properties and relevant mechanisms as land surface conditions are varied. At the highest land albedo values, a monsoon cannot develop regardless of the land moisture condition, resulting in mean descent. Over dry land at mid-range land albedo values, a very shallow thermally driven monsoon develops. As land albedo decreases further, increasing the net column forcing and the cross-equatorial near-surface pressure gradient, inertial instability develops and leads to a deeper overturning cell. Deep convection can only develop when the land moisture constraint is relaxed, allowing latent heat fluxes to trigger convective instability. It is worthwhile to note that the shallow, thermally driven circulations resemble the regime described by Lindzen and Nigam (1987) in which boundary layer momentum dynamics play a crucial role. This view is supported by a set of perturbation experiments in which the land surface momentum roughness length is varied from  $5 \times 10^{-5}$  to 0.5 meters (its default value is  $5 \times 10^{-3}$ ). When land surface roughness is increased by four orders of magnitude, precipitation

617 increases strongly in D0.26 (+38%), slightly less so in R0.26 (+32%), and negligibly in W0.26  
618 (+3.7%).

619 The mechanisms at play in the idealized model simulations as land properties are modified  
620 may be relevant for the seasonal development of monsoons on Earth. Inertial instability alone  
621 is sufficient for producing a shallow but vigorous circulation and converging a large amount of  
622 moisture from the ocean. This mechanism may be key to monsoon onset following the dry season  
623 when soil moisture is low. Once the land is sufficiently moist, convective instability takes hold; the  
624 shallow circulation turns into a deep one. This mechanistic sequence is consistent with previous  
625 arguments (e.g. Fu et al. 1999) that wet season South American precipitation develops only after  
626 sufficient low-level moisture convergence reduces the convective inhibition.

627 In addition to elucidating the seasonal evolution of monsoon circulations, the idealized exper-  
628 iments indicate bounds on the range of land surface conditions that might support a monsoonal  
629 climate. When the net forcing is negative or the near-surface MSE is below the tropical mean  
630 value, a monsoon does not develop. It will be interesting to evaluate such threshold behavior in  
631 more realistic modeling settings. This can illuminate historical changes in tropical hydroclimate  
632 and provides a basis for understanding the how rising carbon dioxide levels may impact monsoons  
633 via their effect on land surface conditions.

634 *Acknowledgments.* Thanks to Spencer Clark for his help running the idealized moist model. We  
635 also thank Spencer Hill and Spencer Clark, developers of the “aospy” climate model analysis  
636 package for Python. When published, model output will be made available at [osf.io](https://osf.io).

## 637 **References**

638 An, Z., and Coauthors, 2015: Global monsoon dynamics and climate change. *Annual Review of*  
639 *Earth and Planetary Sciences*, **43**, 29–77.

- Back, L., and C. Bretherton, 2006: Geographic variability in the export of moist static energy and vertical motion profiles in the tropical pacific. *Geophysical research letters*, **33** (17).
- Berg, A., B. Lintner, K. Findell, S. Seneviratne, and B. van den Hurk et al., 2015: Interannual coupling between summertime surface temperature and precipitation over land: Processes and implications for climate change. *J. Climate*, **28**, 1308–1328.
- Boos, W. R., and T. Storelvmo, 2016: Near-linear response of mean monsoon strength to a broad range of radiative forcings. *Proceedings of the National Academy of Sciences*, **113** (6), 1510–1515.
- Bordoni, S., and T. Schneider, 2008: Monsoons as eddy-mediated regime transitions of the tropical overturning circulation. *Nature Geoscience*, **1** (8), 515–519.
- Bretherton, C. S., P. N. Blossey, and M. E. Peters, 2006: Interpretation of simple and cloud-resolving simulations of moist convection–radiation interaction with a mock-walker circulation. *Theoretical and Computational Fluid Dynamics*, **20** (5-6), 421–442.
- Byrne, M. P., and P. A. O’Gorman, 2013: Land–ocean warming contrast over a wide range of climates: convective quasi-equilibrium theory and idealized simulations. *Journal of Climate*, **26** (12), 4000–4016.
- Byrne, M. P., and P. A. O’Gorman, 2015: The response of precipitation minus evapotranspiration to climate warming: Why the “wet-get-wetter, dry-get-drier” scaling does not hold over land. *Journal of Climate*, **28** (20), 8078–8092, doi:10.1175/JCLI-D-15-0369.1.
- Chao, W. C., and B. Chen, 2001: The origin of monsoons. *Journal of the Atmospheric Sciences*, **58** (22), 3497–3507.

661 Charney, J. G., 1975: Dynamics of deserts and drought in the sahel. *Quarterly Journal of the Royal*  
662 *Meteorological Society*, **101 (428)**, 193–202.

663 Charney, J. G., and M. Stern, 1962: On the stability of internal baroclinic jets in a rotating atmo-  
664 sphere. *Journal of the Atmospheric Sciences*, **19 (2)**, 159–172.

665 Chou, C., and J. D. Neelin, 2001: Mechanisms limiting the southward extent of the south american  
666 summer monsoon. *Geophysical research letters*, **28 (12)**, 2433–2436.

667 Chou, C., and J. D. Neelin, 2004: Mechanisms of global warming impacts on regional tropical  
668 precipitation. *Journal of Climate*, **17 (13)**, 2688–2701.

669 Clark, S. K., Y. Ming, and Á. F. Adames, 2020: Monsoon low pressure system–like variability in  
670 an idealized moist model. *Journal of Climate*, **33 (6)**, 2051–2074.

671 Clark, S. K., Y. Ming, I. M. Held, and P. J. Phillipps, 2018: The role of the water vapor feedback  
672 in the itcz response to hemispherically asymmetric forcings. *Journal of Climate*, **31 (9)**, 3659–  
673 3678.

674 Emanuel, K. A., 1995: On thermally direct circulations in moist atmospheres. *Journal of the*  
675 *atmospheric sciences*, **52 (9)**, 1529–1534.

676 Emanuel, K. A. J. D. N., and C. S. Bretherton, 1994: On large-scale circulations in convecting  
677 atmospheres. *Quarterly Journal of the Royal Meteorological Society*, **120 (519)**, 1111–1143.

678 Frierson, D., 2007: The dynamics of idealized convection schemes and their effect on the zonally  
679 averaged tropical circulation. *Journal of the Atmos. Sciences*, **64**, 1959–1975.

680 Frierson, D. M., I. M. Held, and P. Zurita-Gotor, 2006: A gray-radiation aquaplanet moist gcm.  
681 part i: Static stability and eddy scale. *Journal of the atmospheric sciences*, **63 (10)**, 2548–2566.

682 Fu, R., and W. Li, 2004: The influence of the land surface on the transition from dry to  
683 wet season in amazonia. *Theoretical and Applied Climatology*, **78** (1), 97–110, doi:10.1007/  
684 s00704-004-0046-7.

685 Fu, R., B. Zhu, and R. E. Dickinson, 1999: How do atmosphere and land surface influence seasonal  
686 changes of convection in the tropical amazon? *Journal of Climate*, **12** (5), 1306–1321.

687 Garreaud, R., and P. Aceituno, 2001: Interannual rainfall variability over the south american alti-  
688 plano. *Journal of climate*, **14** (12), 2779–2789.

689 Geen, R., S. Bordoni, D. S. Battisti, and K. Hui, 2020: Monsoons, itczs and the concept of the  
690 global monsoon. *Reviews of Geophysics*, e2020RG000700.

691 Harrop, B. E., J. Lu, and L. R. Leung, 2019: Sub-cloud moist entropy curvature as a predictor for  
692 changes in the seasonal cycle of tropical precipitation. *Climate Dynamics*, **53** (5), 3463–3479.

693 Hill, S. A., 2019: Theories for past and future monsoon rainfall changes. *Journal of Climate*, **5** (3),  
694 160–171.

695 Hill, S. A., Y. Ming, I. M. Held, and M. Zhao, 2017: A moist static energy budget–based analysis  
696 of the sahel rainfall response to uniform oceanic warming. *Journal of Climate*, **30** (15), 5637–  
697 5660.

698 Hsieh, J., and K. H. Cook, 2005: Generation of african easterly wave disturbances: Relationship  
699 to the african easterly jet. *Mon. Wea. Rev.*, **133**, 1311–1327.

700 Hurley, J., and W. Boos, 2013: Interannual variability of monsoon precipitation and local subcloud  
701 equivalent potential temperature. *Journal of Climate*, **26** (23), 9507–9527.



- 702 Kodama, Y., 1992: Large-scale common features of subtropical precipitation zones (the baiu  
703 frontal zone, the spcz, and the sacz) part i: Characteristics of subtropical frontal zones. *Journal*  
704 *of the Meteorological Society of Japan. Ser. II*, **70 (4)**, 813–836.
- 705 Kodama, Y.-M., 1993: Large-scale common features of sub-tropical convergence zones (the baiu  
706 frontal zone, the spcz, and the sacz) part ii: conditions of the circulations for generating the  
707 stczs. *Journal of the Meteorological Society of Japan. Ser. II*, **71 (5)**, 581–610.
- 708 Koster, R. D., and Coauthors, 2004: Regions of strong coupling between soil moisture and precip-  
709 itation. *Science*, **305 (5687)**, 1138–1140.
- 710 Levine, X. J., and W. R. Boos, 2017: Land surface albedo bias in climate models and its association  
711 with tropical rainfall. *Geophysical Research Letters*, **44 (12)**, 6363–6372.
- 712 Lindzen, R. S., and S. Nigam, 1987: On the role of sea surface temperature gradients in forcing  
713 low-level winds and convergence in the tropics. *Journal of the Atmospheric Sciences*, **44 (17)**,  
714 2418–2436.
- 715 Manabe, S., 1969: Climate and the ocean circulation: I. the atmospheric circulation and the hy-  
716 drology of the earth's surface. *Monthly Weather Review*, **97 (11)**, 739–774.
- 717 Maroon, E. A., and D. M. Frierson, 2016: The impact of a continent's longitudinal extent on  
718 tropical precipitation. *Geophysical Research Letters*, **43 (22)**, 11–921.
- 719 Neelin, D., and I. Held, 1987: Modeling tropical convergence based on the moist static energy  
720 budget. *Mon. Wea. Rev.*, **115**, 3–12.
- 721 Neelin, J. D., 2007: Moist dynamics of tropical convection zones in monsoons, teleconnections,  
722 and global warming. Princeton University Press, 267–301 pp.

723 Nie, J., W. R. Boos, and Z. Kuang, 2010: Observational evaluation of a convective quasi-  
724 equilibrium view of monsoons. *Journal of Climate*, **23** (16), 4416–4428.

725 Nieto Ferreira, R., and W. C. Chao, 2013: Aqua-planet simulations of the formation of the south  
726 atlantic convergence zone. *International journal of climatology*, **33** (3), 615–628.

727 Paynter, D., and V. Ramaswamy, 2014: Investigating the impact of the shortwave water vapor con-  
728 tinuum upon climate simulations using gfdl global models. *Journal of Geophysical Research:*  
729 *Atmospheres*, **119** (18), 10–720.

730 Plumb, R. A., and A. Y. Hou, 1992: The response of a zonally symmetric atmosphere to sub-  
731 tropical thermal forcing: Threshold behavior. *Journal of the atmospheric sciences*, **49** (19),  
732 1790–1799.

733 Privé, N. C., and R. A. Plumb, 2007a: Monsoon dynamics with interactive forcing. part i: Ax-  
734 isymmetric studies. *Journal of the atmospheric sciences*, **64** (5), 1417–1430.

735 Privé, N. C., and R. A. Plumb, 2007b: Monsoon dynamics with interactive forcing. part ii: Impact  
736 of eddies and asymmetric geometries. *Journal of the atmospheric sciences*, **64** (5), 1431–1442.

737 Schwingshackl, C., M. Hirschi, and S. I. Seneviratne, 2018: A theoretical approach to assess soil  
738 moisture-climate coupling across cmip5 and glace-cmip5 experiments. *Earth System Dynamics*,  
739 **9** (4), 1217–1234.

740 Seneviratne, S. I., T. Corti, E. L. Davin, M. Hirschi, E. B. Jaeger, I. Lehner, B. Orlowsky, and A. J.  
741 Teuling, 2010: Investigating soil moisture–climate interactions in a changing climate: A review.  
742 *Earth-Science Reviews*, **99** (3-4), 125–161.

743 Sharma, O., H. Le Treut, G. Seze, L. Fairhead, and R. Sadourny, 1998: Interannual variations  
 744 of summer monsoons: Sensitivity to cloud radiative forcing. *Journal of climate*, **11** (8), 1883–  
 745 1905.

746 Skinner, C. B., and N. S. Diffenbaugh, 2014: Projected changes in african easterly wave intensity  
 747 and track in response to greenhouse forcing. *Proceedings of the National Academy of Sciences*,  
 748 **111** (19), 6882–6887.

749 Smyth, J., S. Hill, and Y. Ming, 2018: Simulated responses of the west african monsoon and zonal-  
 750 mean tropical precipitation to early holocene orbital forcing. *Geophysical Research Letters*, **45**,  
 751 12,049– 12,057, doi:10.1029/2018GL080494.

752 Smyth, J. E., and Y. Ming, 2020: Characterizing drying in the south american monsoon onset  
 753 season with the moist static energy budget. *Journal of Climate*, 1–41.

754 Tomas, R. A., and P. J. Webster, 1997: The role of inertial instability in determining the loca-  
 755 tion and strength of near-equatorial convection. *Quarterly Journal of the Royal Meteorological*  
 756 *Society*, **123** (542), 1445–1482.

757 Vallis, G. K., and Coauthors, 2018: Isca, v1. 0: A framework for the global modelling of the  
 758 atmospheres of earth and other planets at varying levels of complexity.

759 Van Der Wiel, K., A. J. Matthews, D. P. Stevens, and M. M. Joshi, 2015: A dynamical framework  
 760 for the origin of the diagonal south pacific and south atlantic convergence zones. *Quarterly*  
 761 *Journal of the Royal Meteorological Society*, **141** (691), 1997–2010.

762 Voigt, A., S. Bony, J.-L. Dufresne, and B. Stevens, 2014: The radiative impact of clouds on the  
 763 shift of the intertropical convergence zone. *Geophysical Research Letters*, **41** (12), 4308–4315.

- 764 Walker, J. M., S. Bordoni, and T. Schneider, 2015: Interannual variability in the large-scale dy-  
765 namics of the south asian summer monsoon. *Journal of Climate*, **28** (9), 3731–3750.
- 766 Wang, H., and R. Fu, 2004: Influence of cross-andes flow on the south american low-level jet.  
767 *Journal of climate*, **17** (6), 1247–1262.
- 768 Zhai, J., and W. Boos, 2015: Regime transitions of cross-equatorial hadley circulations with zon-  
769 ally asymmetric thermal forcings. *Journal of the Atmospheric Sciences*, **72** (10), 3800–3818.
- 770 Zhang, Y., and S. Fueglistaler, 2020: How tropical convection couples high moist static energy  
771 over land and ocean. *Geophysical Research Letters*, **47** (2), e2019GL086387.
- 772 Zhou, W., and S.-P. Xie, 2018: A hierarchy of idealized monsoons in an intermediate gcm. *Journal*  
773 *of Climate*, **31** (22), 9021–9036.

774 **LIST OF TABLES**

775 **Table 1.** JFM column-integrated MSE budget terms ( $\text{W m}^{-2}$ ) averaged over the South  
 776 American monsoon sector in the D0.26, R0.26, and W0.26 experiments. . . . . 38

777 TABLE 1. JFM column-integrated MSE budget terms ( $\text{W m}^{-2}$ ) averaged over the South American monsoon  
778 sector in the D0.26, R0.26, and W0.26 experiments.

	D0.26	R0.26	W0.26
$\bar{F}_{net}$	7.8	50.3	64.3
$\frac{\partial}{\partial t}\{\bar{\mathcal{E}}\}$	3.5	3.6	3.1
$\{\bar{\mathbf{v}} \cdot \nabla_p \bar{h}\}$	5.8	9.9	6.2
$\left\{\bar{\omega} \frac{\partial \bar{h}}{\partial p}\right\}$	-23.6	21.7	43.4
$\nabla \cdot \{\bar{h} \nabla\}$	20.6	13.7	12.1

## LIST OF FIGURES

779	<b>Fig. 1.</b>	Seasonal cycles of region-mean (a) precipitation, (b) surface temperature and insolation, and (c) net precipitation ( $P - E$ ) over the South American monsoon sector in the D0.26, R0.26, and W0.26 experiments. . . . .	40
780			
781	<b>Fig. 2.</b>	JFM mean distributions of precipitation (shading) in $\text{mm d}^{-1}$ and 973 hPa MSE (contours) in Kelvin in the (a) D0.26, (b) R0.26, and (c) W0.26 simulations and (d) GPCP v2.3 1997-2015 precipitation observations. The green box outlines the monsoon sector . . . . .	41
782			
783	<b>Fig. 3.</b>	JFM mean distributions of 920 hPa specific humidity (shading) and horizontal winds (vectors) in (a) D0.26, (b) R0.26, and (c) W0.26 and at 925 hPa and for (d) ERA-Interim re-analysis, interpolated to the idealized model grid resolution. The model results (a-c) use the colorbar below subplot (c). The magenta box denotes the monsoon sector. . . . .	42
784			
785	<b>Fig. 4.</b>	JFM monsoon sector-mean vertical profiles of (a) vertical pressure velocity, (b) MSE, (c) DSE, (d) specific humidity, and (e) relative humidity in the three baseline experiments. . . . .	43
786			
787	<b>Fig. 5.</b>	JFM distributions of the near-surface (973 hPa) MSE minus the tropical mean ( $30^\circ \text{ S}$ to $30^\circ \text{ N}$ ) value (shading) and precipitation in $\text{mm d}^{-1}$ (contours) in each of the three baseline experiments. The green box outlines the monsoon sector. . . . .	44
788			
789	<b>Fig. 6.</b>	JFM mean precipitation in the monsoon sector as a function of land surface albedo with dry, wet, and realistic surface moisture conditions. The black arrow indicates the control albedo value of 0.26. . . . .	45
790			
791	<b>Fig. 7.</b>	JFM mean vertical profiles of the vertical pressure velocity over the monsoon sector as land surface albedo is varied in the (a) dry, (b) realistic, and (c) wet land surface moisture experimental suites. . . . .	46
792			
793	<b>Fig. 8.</b>	February 920 hPa absolute vorticity (contours) and divergence (shading) in the (a) D0.1, (b) D0.3, (c) D0.4, and (d) D0.5 simulations. The bold black line is the zero-line of absolute vorticity. The green box outlines the monsoon sector. . . . .	47
794			
795	<b>Fig. 9.</b>	JFM mean precipitation in the monsoon sector as a function of (a) net column energy and (b) 973 hPa $\theta_e$ in all land surface albedo and moisture perturbation experiments. Panel (a) also includes the data for all four seasons of the GFDL AM4 control and +2-K SST warming experiments (labeled on the plot), as well as the four seasons of the D0.26 experiment (JFM, AMJ, JAS, OND). Panel (b) includes the seasonal data for the three baseline experiments. . . . .	48
796			
797	<b>Fig. 10.</b>	A schematic overview of the monsoon circulation properties and relevant physical mechanisms across the land surface parameter space. . . . .	49
798			
799			
800			
801			
802			
803			
804			
805			
806			
807			
808			
809			
810			

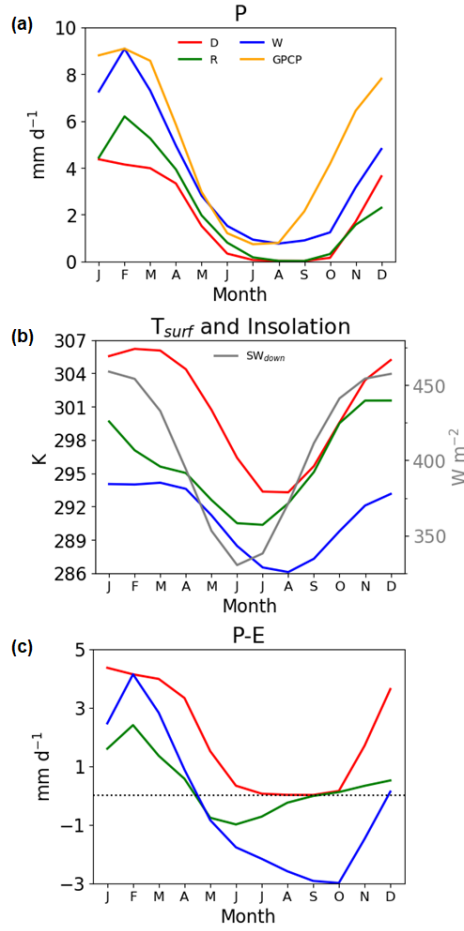
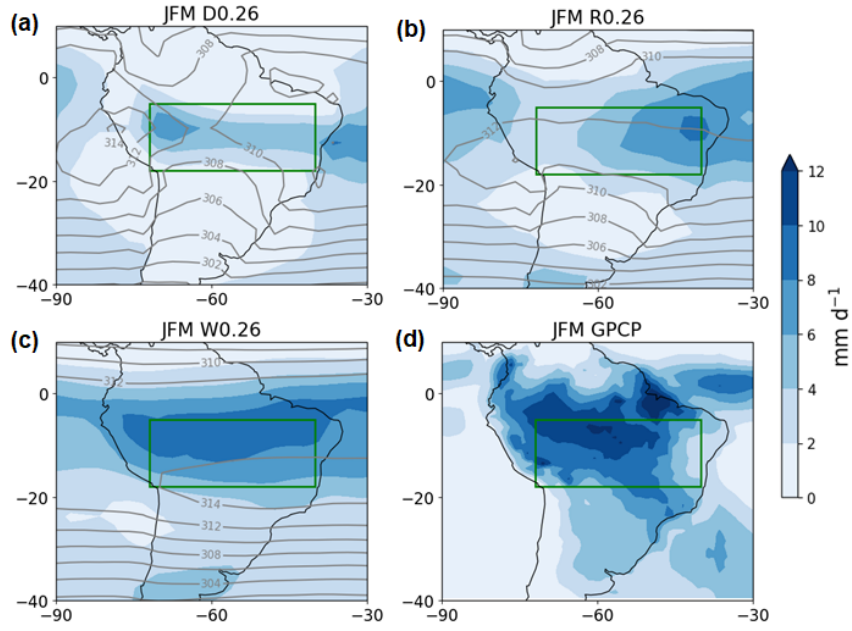
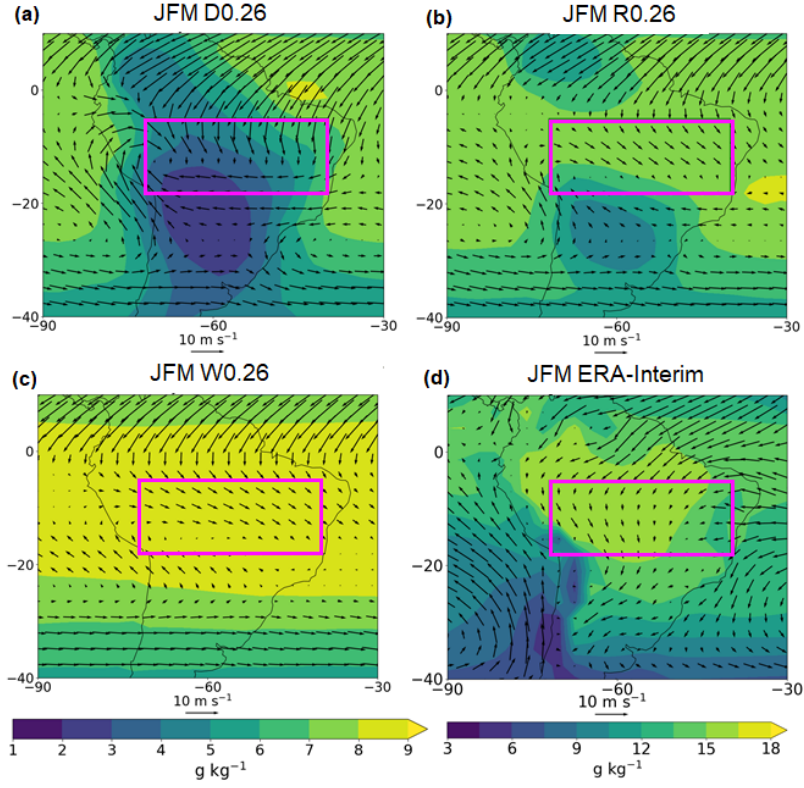


FIG. 1. Seasonal cycles of region-mean (a) precipitation, (b) surface temperature and insolation, and (c) net precipitation ( $P - E$ ) over the South American monsoon sector in the D0.26, R0.26, and W0.26 experiments.





813 FIG. 2. JFM mean distributions of precipitation (shading) in  $\text{mm d}^{-1}$  and 973 hPa MSE (contours) in Kelvin  
 814 in the (a) D0.26, (b) R0.26, and (c) W0.26 simulations and (d) GPCP v2.3 1997-2015 precipitation observations.  
 815 The green box outlines the monsoon sector



816 FIG. 3. JFM mean distributions of 920 hPa specific humidity (shading) and horizontal winds (vectors) in (a)  
 817 D0.26, (b) R0.26, and (c) W0.26 and at 925 hPa and for (d) ERA-Interim reanalysis, interpolated to the idealized  
 818 model grid resolution. The model results (a-c) use the colorbar below subplot (c). The magenta box denotes the  
 819 monsoon sector.

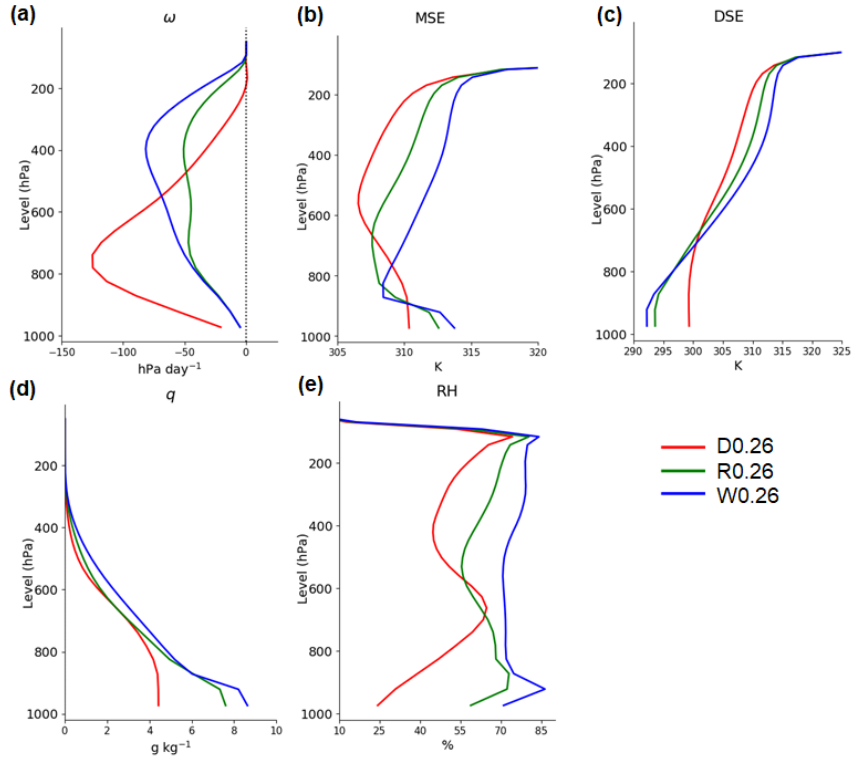


FIG. 4. JFM monsoon sector-mean vertical profiles of (a) vertical pressure velocity, (b) MSE, (c) DSE, (d) specific humidity, and (e) relative humidity in the three baseline experiments.

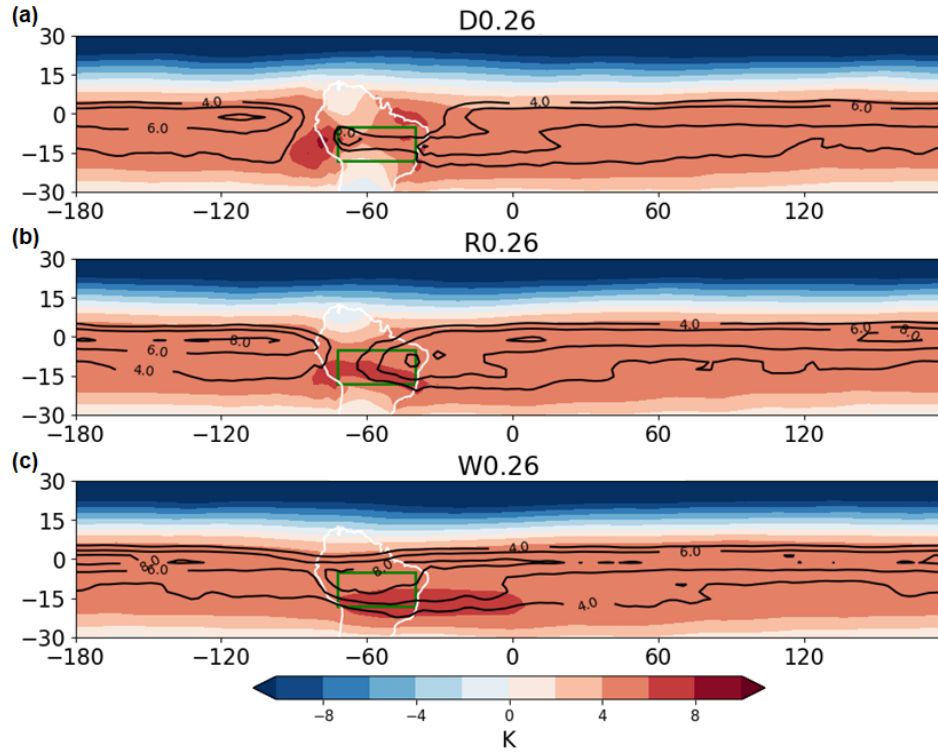


FIG. 5. JFM distributions of the near-surface (973 hPa) MSE minus the tropical mean (30° S to N) value (shading) and precipitation in mm d<sup>-1</sup> (contours) in each of the three baseline experiments. The green box outlines the monsoon sector.

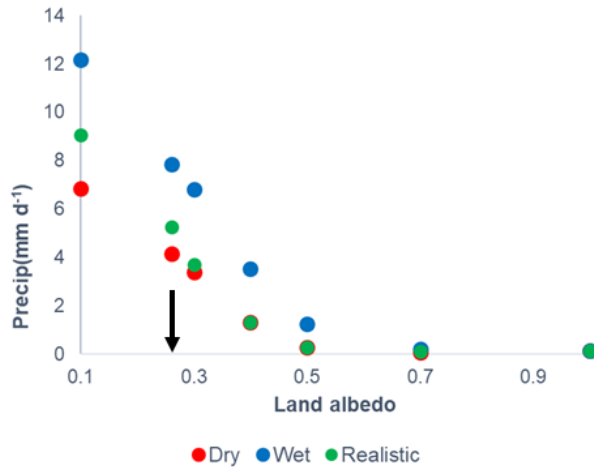


FIG. 6. JFM mean precipitation in the monsoon sector as a function of land surface albedo with dry, wet, and realistic surface moisture conditions. The black arrow indicates the control albedo value of 0.26.

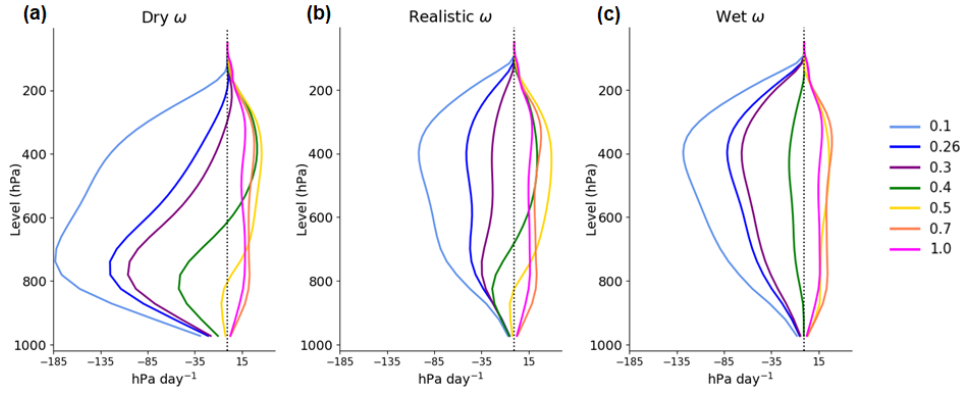
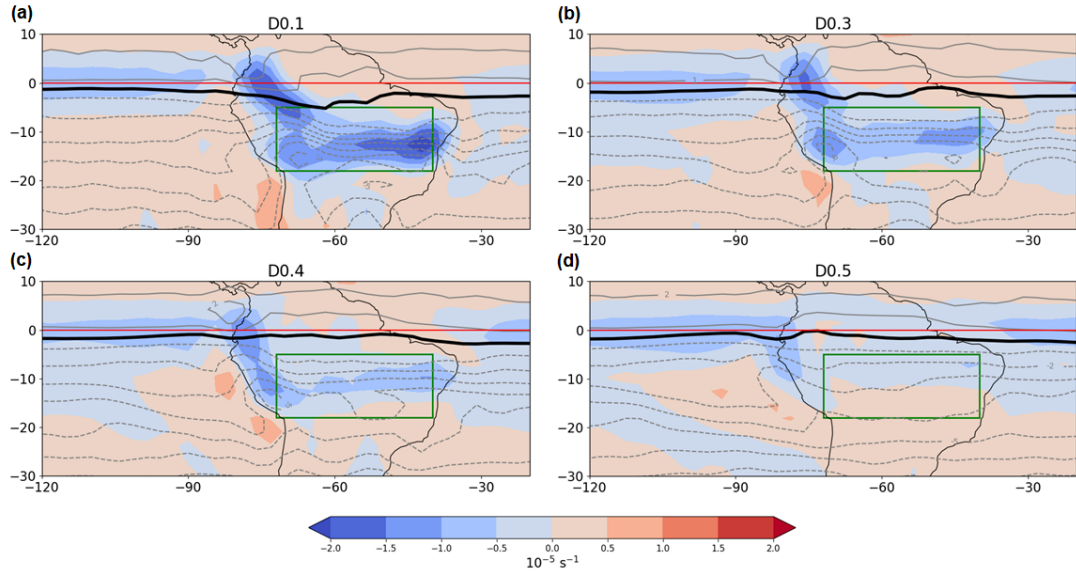


FIG. 7. JFM mean vertical profiles of the vertical pressure velocity over the monsoon sector as land surface albedo is varied in the (a) dry, (b) realistic, and (c) wet land surface moisture experimental suites.



829 FIG. 8. February 920 hPa absolute vorticity (contours) and divergence (shading) in the (a) D0.1, (b) D0.3, (c)  
 830 D0.4, and (d) D0.5 simulations. The bold black line is the zero-line of absolute vorticity. The green box outlines  
 831 the monsoon sector.

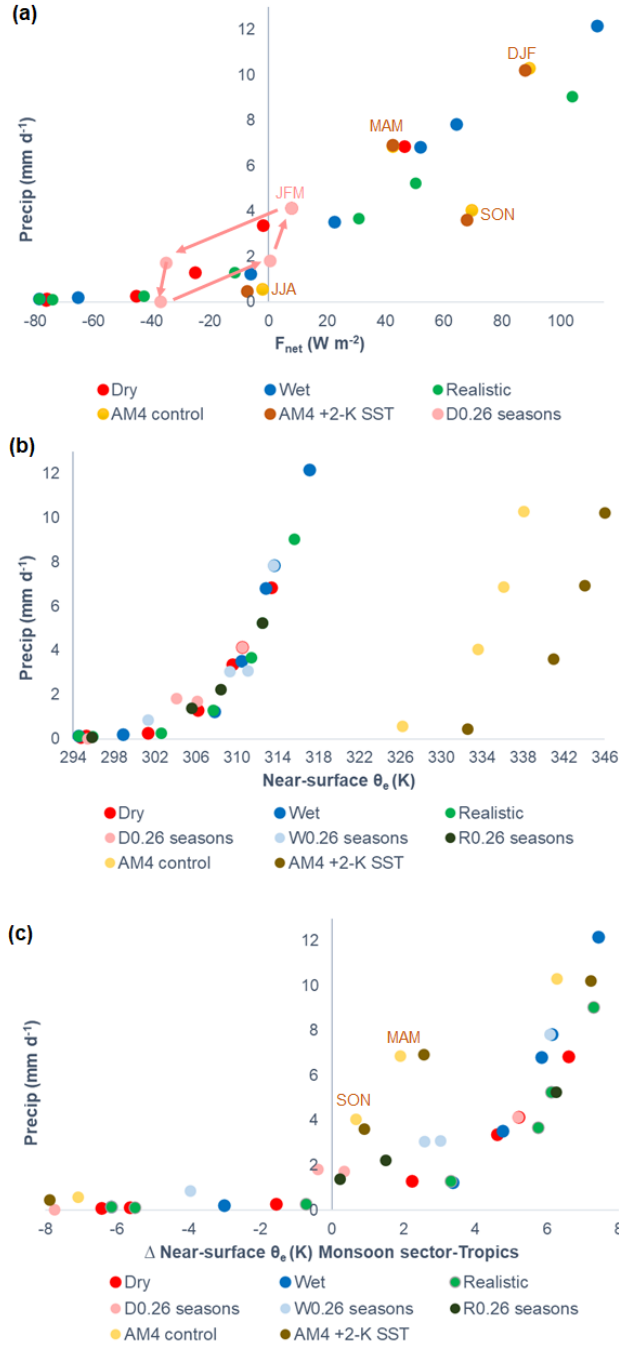
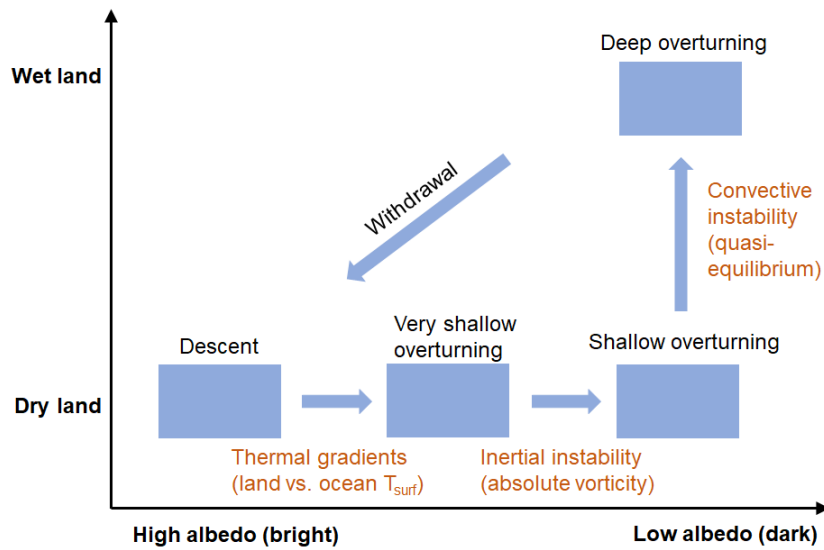


FIG. 9. JFM mean precipitation in the monsoon sector as a function of (a) net column energy and (b) 973 hPa  $\theta_e$  in all land surface albedo and moisture perturbation experiments. Panel (a) also includes the data for all 833 four seasons of the GFDL AM4 control and +2-K SST warming experiments (labeled on the plot), as well as the 834 four seasons of the D0.26 experiment (JFM, AMJ, JAS, OND). Panel (b) includes the seasonal data for the three 835 baseline experiments. 836





837 FIG. 10. A schematic overview of the monsoon circulation properties and relevant physical mechanisms  
 838 across the land surface parameter space.